Integrating pore interconnectivity and adaptability in a single crystal hierarchical zeolite for liquid alkylation

Integrating Pore Interconnectivity and Adaptability in a Single Crystal Hierarchical Zeolite for Liquid Alkylation

Baoyu Liu[*,†], Jiajin Huang[†], Zhantu Liao[†], Chongzhi Zhu[‡], Qiaoli Chen[‡], Guan Sheng[⊥], Yihan Zhu[*,‡], Yi Huang[#] and Jinxiang Dong[†,§]

[†]School of Chemical Engineering and Light Industry, Guangzhou Key Laboratory of Clean Transportation Energy Chemistry, Guangdong University of Technology, Guangzhou, 510006, P.R. China

[‡]Center for Electron Microscopy, State Key Laboratory Breeding Base of Green Chemistry Synthesis Technology and College of Chemical Engineering, Zhejiang University of Technology, Hangzhou, 310014, P.R.China

[⊥]Advanced Membranes and Porous Materials Center, Physical Science and Engineering, King Abdullah University of Science and Technology, Thuwal, 23955-6900, Kingdom of Saudi Arabia

[#]School of Engineering, Institute for Materials & Processes (IMP), The University of Edinburgh, Edinburgh, EH9 3FB, UK

[§]College of Chemistry and Chemical Engineering, Taiyuan University of Technology, Taiyuan, 030024, P.R. China

Abstract

Zeolite belongs to one of the most important families of solid acid catalysts in chemical industries. It is, however, severely constrained by the diffusion limitation for bulky molecules, a lack of multifunctionality for sequential reactions and pore adaptability towards specific adsorbates due to its small micropore size and simple aluminosilicate framework. Introducing mesopores into a zeolite towards realizing hierarchical zeolites is a prevailing strategy but one that usually suffers from compromised crystallinity as well as insufficient interconnectivity and openness of the mesopores. Herein, a novel acid-redox co-functionalized single-crystalline zeolite with highly open and interconnected mesopores is designed and fabricated. As a proof-of-concept study, we integrate solid acid and Fe-oxy redox sites into a

[*] Corresponding author, Email: baoyu.liu@gdut.edu.cn (Baoyu Liu)
[*] Corresponding author, Email: yihanzhu@zjut.edu.cn (Yihan Zhu)

hierarchical MEL zeolite with well-characterized microporosity and mesoporosity. This zeolite exhibits superior activity and stability towards alkylation between mesitylene with benzyl alcohol, arising from greatly facilitated intra-crystal molecular diffusion, mitigated metal leaching and optimized adsorbate-pore wall interactions.

Keywords: Synthesis; MEL Zeolite; Diffusion; Alkylation; Catalysis

Introduction

The alkylation of mesitylene with benzyl alcohol is an important reaction for producing valuable chemicals used for aviation fuel additive reagents, dyes, pharmaceuticals, electrolytes and cosmetics.[1,2] However, this reaction is traditionally catalyzed by homogeneous catalysts such as $AlCl_3$, H_2SO_4 and BF_3,[3,4] which results in many problems such as pollution, corrosion and separation.[5] Heterogeneous solid acid catalysts, especially zeolites with a versatile solid acid and tunable architecture, are highly desired towards realizing a "green" approach for the alkylation of mesitylene.[6] A major concern for conventional zeolite lies in the severe diffusion limitation arising from a small pore size and rigorous coking problem.[7] Hierarchical zeolites with both microporosity and mesoporosity should, in principle, enable one to largely circumvent the diffusion limitation.[8-11] However, zeolites with polycrystalline mesopore walls usually show a compromised framework acidity and stability.[12] Hierarchical single-crystalline zeolites can well retain these properties,[13-15] while the "quality" (i.e., the interconnectivity and surface openness) of the intracrystalline mesopores remains largely unevaluated and those constricted or closed ones are totally inaccessible for bulky molecules.[16,17]

Another important but usually lacking structural feature for the complex porous network of hierarchical zeolites is the adsorbate-specific pore adaptability, which allows further control of product selectivity through largely differentiated adsorbate-pore wall interactions. In addition, it is widely reported that monofunctional acid sites in the zeolite framework exhibit poor activity towards the alkylation of aromatics.[18,19] The loaded redox transition metal additives, such as Fe, Co and Pt, into framework of zeolites can significantly improve the activity of benzylation.[20] However, these strategies often give a low dispersion for metal species, and the loaded metals species are not stable under harsh reaction condition, resulting in sintering and leaching issues.[21] Immobilizing metal species into a zeolite matrix is an effective method to mitigate these problems but is unavailable for conventional chemical synthesis as metal precursors can hardly undergo co-condensation with zeolite precursors instead of forming oxyhydroxide precipitates under the conditions for zeolite synthesis.[22]

In the present research, we developed a simple and general strategy to fabricate a hierarchical single-crystalline MEL zeolite co-functionalized with both solid acid and Fe-oxy redox sites. The Fe species were immobilized into silicate-2 with the assistance of ligand-stabilized iron cations. The subsequent orientated crystal transformation was then accompanied by a targeted leaching-hydrolysis process that finally converted the Fe-containing silicate-2 into acid-redox co-functionalized single crystalline mesoporous MEL zeolites. The single-crystalline/bifunctionalized microporous framework as well as the highly open/interconnected mesoporosity of

the MEL zeolite were unambiguously determined and evaluated by a complementary combination of high-resolution transmission electron microscopy (HRTEM), electron tomography (ET) and positron annihilation lifetime spectroscopy (PALS). A kinetic adsorption experiment further validated the pore adaptability towards nonpolar adsorbates. These unique structural features all together lead to greatly facilitated intracrystalline molecular diffusion, mitigated metal leaching and optimized adsorbate-pore wall interactions towards an excellent overall catalytic performance for the alkylation of aromatics.

Experimental section

Materials

The reagents used in this synthesis process were tetraethyl orthosilicate (TEOS, analytical grade, Damao Chemical Reagent Factory, China), tetrabutylammonium hydroxide (TBAOH, 40 wt % aqueous solution, Energy Chemical, China), aluminum isopropoxide (analytical grade, Aladdin), iron citrate (analytical grade, Aladdin), iron (III) chloride (Adamas-beta), benzyl alcohol (analytical grade, Damao Chemical Reagent Factory, China), and 1,3,5-trimethylbenzene (analytical grade, Aladdin). All water used in the experiment was deionized water.

Catalyst preparation

Pure silica MEL and pure silica Fe containing MEL zeolites were synthesized by a hydrothermal method, using TEOS as a silicon source, iron citrate as the iron source and TBAOH as the organic template, respectively. Typically, the TEOS was slowly added to the TBAOH solution under vigorous stirring, and after mixing at room

temperature for 3 hours, iron citrate and deionized water were added. The final molar composition of the gel was 1 TEOS: 0.25 TBAOH: 25 H_2O: x Fe_2O_3 (x = 0 and 0.007, respectively). After aging for 6 hours at 30 °C, the prepared mixture was placed into a stainless-steel autoclave and crystallized at 170 °C for 72 hours under static conditions. After crystallization, the product was filtered, washed several times with deionized water, and then dried overnight at 100 °C. Finally, the organic templates were removed by calcination at 550 °C for 6 hours in an air atmosphere. These samples were denoted as P-MEL (pure silica MEL zeolite) and P-MEL@Fe (Pure silica Fe containing MEL zeolite), respectively.

The above-synthesized P-MEL and P-MEL@Fe samples were further treated. Typically, a certain amount of aluminum isopropoxide was dissolved in 0.1 M/L of TBAOH solution, and then the concentration of aluminum isopropoxide solution was tuned to 0.015 M/L, 0.024 M/L and 0.03 M/L, respectively. The amount of solution was 30 ml/g of as-prepared P-MEL or P-MEL@Fe. Then, this solution was placed into a stainless-steel autoclave and crystallized at 170 °C for 72 hours under static conditions. In the same way, the product was filtered, washed several times with deionized water, and then dried overnight at 100 °C. Finally, the organic template was removed by calcination at 550 °C for 6 hours in an air atmosphere. These hierarchical zeolites were denoted as H-MEL-31 (which was obtained from P-MEL and the Si/Al = 31) or H-MEL@Fe-34, H-MEL@Fe-23 and H-MEL@Fe-20 (prepared from P-MEL@Fe and Si/Al = 34, 23 and 20, respectively). The corresponding Si/Al ratios for the zeolites were determined by ICP-OES.

Results and discussion

Characterization of zeolites

Figure 1 showed the powder X-ray diffraction (XRD) patterns for various MEL zeolite samples; it was observed that all the synthesized samples exhibited the characteristic peaks (such as 2θ = 7.9°, 8.8°, 14.8°, 23.1° and 23.9°) of an MEL topologic framework,[23,24] indicating that the MEL zeolites were successfully fabricated in the present work. No other detectable diffraction peaks for metal phases, such as large iron oxides, were found, which indicated a substantial absence of large metal crystallites. In addition, EDX mapping (Fig. 2a) further demonstrated that the immobilized Fe species were homogeneously distributed throughout the whole MEL zeolite particle.

The chemical state of these species was characterized by XPS, and the results were displayed in Fig. S1. For Fe-containing MEL zeolites, two peaks were observed at 711.8 eV and 725.4 eV corresponding to $Fe_{2p3/2}$ and $Fe_{2p1/2}$ in Fe^{3+}, respectively.[25,26] Moreover, additional satellite peaks at ~716.3 eV and 729.9 eV were also observed in P-MEL@Fe (Fig. S1a) and H-MEL@Fe-*x* (Fig. S1b-S1d), which represented the binding energies of $Fe_{2p3/2}$ and $Fe_{2p1/2}$ in Fe(III) of Fe_2O_3, respectively.[27] The UV-Vis spectroscopy data for the resultant zeolite samples was given in Fig. S2, and the corresponding percentages for the different iron species of zeolites were listed in Table S1. It was found that Fe^{3+} species were the majority of species. Moreover, EPR analysis was further carried out to detect the structure and coordination environment of Fe species in Fe-containing MEL zeolites, where the two distinct resonance signals

at g = 4.3 and 2.0 referred to Fe^{3+} species in a distorted tetrahedral and a highly symmetric coordination, respectively (Fig. S3).[28,29] Based on the above analysis, it was deduced that most of the iron species loaded in the P-MEL@Fe, H-MEL@Fe-34, H-MEL@Fe-23 and H-MEL@Fe-20 samples existed in the form of Fe(III).

SEM images of as-synthesized MEL zeolites showed a uniform rugby-like morphology (Fig. S4), and P-MEL had a smooth surface. When Fe and Al species were incorporated into the zeolite framework, the samples exhibited a rough surface and some fragments appeared on the surface of the zeolites (Fig. S4b-S4f), but the rugby-like structure was not destroyed. TEM imaging of zeolites was further carried out to investigate the framework structure of the samples, as shown in Fig. S5. It was observed that P-MEL (Fig. S5a) and P-MEL@Fe (Fig. S5c) showed a condensed structure, while the H-MEL-31 and H-MEL@Fe-*x* samples exhibited an unconsolidated structure (Fig. S5b and S5d-S5f). In addition, the electron diffraction pattern for a randomly selected MEL zeolite particle further confirmed its single-crystalline nature (Fig. S6).

N_2 adsorption-desorption isotherms was used to reveal the porosity of resultant MEL zeolites, as shown in Fig. S7. It was observed that H-MEL-31, H-MEL@Fe-34, H-MEL@Fe-23 and H-MEL@Fe-20 showed distinct Type-IV isotherms with a H2 hysteresis loop corresponding to capillary condensation in the mesopores.[30,31] In contrast, the P-MEL and P-MEL@Fe did not show any hysteresis loops owing to the sole micropores. The pore size distribution for the obtained zeolite samples was analyzed by NLDFT (nonlocal density functional theory) and BJH (Barrett–Joyner–

Halenda) methods, respectively, and the data obtained was shown in Fig. S8. All of the samples exhibited a narrow peak at ~0.56 nm, as shown in Fig. S8a, corresponding to the micropore size for the MEL zeolite, while the H-MEL-31, H-MEL@Fe-34, H-MEL@Fe-23 and H-MEL@Fe-20 showed additional broad peaks compared with P-MEL and P-MEL@Fe in the region of 3~4.5 nm,, as shown in Fig. S8b, which was attributed to the formation of a mesoporous structure. The above TEM images, N_2 adsorption data combined with textural properties of the zeolites (Table S2) verified that the H-MEL-31 and H-MEL@Fe-*x* zeolites encompassed a significant amount of mesoporosity, possibly arising from the orientated crystal transformation process：i) the silica source (TEOS) and template (TBAOH) assembled with ferric citrate through the electrostatic and dispersion interactions between zeolite precursor and solvated ligand-stabilized Fe species[22], inducing the formation of Fe-containing silicate-2; ii) this Fe-containing silicate-2 underwent targeted corrosion towards silicon extraction by interactions between Si–OH groups on the surface of the silicate-2 and TBA^+, resulting in the generation of voids in the silicate-2[32]. Simultaneously, the Fe-containing silicate-2 completed crystal transformation *via* directional control of the crystallization process combined with leached silicate oligomers and additional aluminum isopropoxide species, guiding the formation of acid-redox co-functionalized single crystalline mesoporous MEL zeolites, as schematically illustrated in Scheme 1. These mesopores were enclosed by a series of low-index facets such as [011] and [010], as clearly observed in HRTEM images from an “edge-on” projection (Fig. 2b and 2c). After correcting for defocus effects (Fig. 2d),

The HRTEM images of the crystalline pore walls also well matched the simulated projected potential and structural projections for an MEL zeolite along the [100] direction.

The “quality” of these intracrystalline mesoporosity, in terms of interconnectivity and openness, can be directly evaluated in three-dimensions and real-space by ET. Based on a TEM tilt series for H-MEL-31 as a typical mesoporous MEL zeolite, the reconstructed 3D tomogram can be visualized through volume rendering as shown in Fig. 3a and Fig. S9. From the 3D tomogram, the intracrystalline mesoporosity can be directly identified, which can even be more clearly observed from sequential slices of the tomogram, as shown in Fig. 3 h. These slices with an interval of 10 nm exhibited highly interconnected voids either within or between individual slices, implying a high degree of 3D interconnectivity for the mesopores. A thorough segmentation of the tomogram allowed for precise 3D labeling of individual interconnected mesopores with different sizes and shapes, as shown in Fig. 3b-3f (rendered with different colors). These labeled mesopores can be further classified according to their different equivalent spherical pore sizes and quantified statistically in a bar chart, as shown in Fig. 3i. Among these mesopores, those connected to the surface can be further labeled and quantified, as shown in Fig. 3 g & 3i, which were defined as “open mesopores” (otherwise “constricted” or “closed” mesopores). Accordingly, it can be observed that a majority of the interconnected intracrystalline mesopores were highly open to the surface (Fig. 3i). Moreover, positron annihilation lifetime spectroscopy (PALS) was further employed to verify the pore connectivity of the zeolites due to its

unprecedented sensitivity towards the bulk connectivity of the complex pore network. The normalized PALS spectra and corresponding lifetime components with relative fractions of P-MEL and H-MEL-31 were shown in Fig. 4a and Fig. 4b, respectively. It was observed from Fig. 4b that the P-MEL exhibited higher fractions of o-Ps annihilating in the micro- and mesopores compared to H-MEL-31, which was indicative of increased resistance for o-Ps migration from both micropores-to-mesopores and micropores/mesopores-to-vacuum.[16] While the high fraction of o-Ps annihilating in vacuum for the hierarchically structured H-MEL-31 compared with P-MEL suggested that H-MEL-31 possessed superior interconnectivity for the micro- and mesopore network and surface openness, which greatly promotes intracrystalline molecular transport.[17]

Acidity of zeolites

In general, the acidity of zeolites arises from the Al species that are substituted for tetrahedral Si atoms in the framework, which gives rise to Brønsted acid sites and Lewis acid sites depending on the different Al-coordinated environments.[33] The MEL zeolite contains 7 crystallographically distinct T sites, as shown in Fig. 5 and Fig. S10. Here, the acidity of synthesized samples was evaluated from the IR spectra for pyridine/2,6-di-tert-butyl pyridine adsorption onto the H^+-form of zeolites. The pyridine with a kinetic diameter of ~ 0.5 nm can enter the channel of MEL (0.53 × 0.54 nm).[34] Thus, it can detect the total acidity of the zeolites. Figure S11a exhibited the IR spectra for adsorbed pyridine over the investigated samples; it was known that the absorption bands at ~ 1546 cm^{-1} and 1446 cm^{-1} can be attributed to Brønsted acid

sites and Lewis acid sites, respectively,[35,36] and the corresponding acidity of the zeolites was listed in Table S3. As shown in Table S3, P-MEL and P-MEL@Fe did not show any Brønsted acidity due to the absence of Al species in the framework of the MEL zeolites. After incorporating Al into the zeolite lattice, the Brønsted acidity of the samples gradually increased. For example, the Brønsted acidity of P-MEL@Fe and H-MEL@Fe-*x* increased in the order of P-MEL@Fe < H-MEL@Fe-34 < H-MEL@Fe-23 < H-MEL@Fe-20, which indicated that Al species preferred to exist in the form of Si–OH^+–Al, resulting in the generation of Brønsted acid sites. In addition, P-MEL@Fe showed a higher Lewis acidity than that for P-MEL owing to the additional Fe species that can become Lewis acid sites by accepting a pair of electrons from the adsorbed species.[37]

It was difficult for 2,6-di-tert-butyl pyridine (2,6-DTBPy) with a kinetic diameter of ~0.8 nm to enter the MEL zeolite channel, therefore, it can be used to test the acidity on the mesopores surface of zeolites. As shown in Fig. S11b, the band at ~1616 cm^{-1} was characteristic of Brønsted acid sites, which can catalyze the alkylation between mesitylene (kinetic diameter of ~0.87 nm) and benzyl alcohol. Table S3 gave the mesopores surface Brønsted acidity of zeolites; it was observed that P-MEL and P-MEL@Fe did not show any mesopores surface Brønsted acidity owing to the missing Al species. However, the concentration of Brønsted acid of H-MEL@Fe-*x* on the mesopores surface increased with decreasing Si/Al ratio, and the Brønsted acid/Lewis acid ratios for H-MEL@Fe-*x* also exhibited a similar trend with the Si/Al ratios, indicating that the Brønsted acid/Lewis acid ratios and

mesopores surface Brønsted acidity of H-MEL@Fe-*x* can be modulated by tuning the Si/Al ratio of the zeolites, which is important for tailoring the catalytic properties of zeolite catalysts.

Analysis of diffusion

In addition to the above effects arising from pore size, pore interconnectivity and surface openness, the chemical environment of the internal pore wall also plays a critical role in determining the overall molecular diffusion properties. Kinetic adsorption experiments over diverse probe molecules allow for unambiguous discrimination between intra-crystalline and inter-crystal diffusion events.[38] Hereby, effects arising from electrostatic interaction between the internal/external surface and adsorbate were investigated over nonpolar benzene and polar toluene molecules with a similar kinetic diameter (~ 0.56 nm) to that of the channel size of the MEL (0.53 × 0.54 nm) respectively. These two selected probe molecules were also free of functional groups, which avoided any potential chemical bonding with the surface. Figure 6(a, b) showed plots of transient fractional uptake $[(Q_t-Q_0)/(Q_e-Q_0)]$ of benzene and toluene versus square root of time in H-MEL-31, P-MEL@Fe and H-MEL@Fe-20 at 35 °C, respectively. Briefly, the logarithm of the normalized transient fractional uptake $[(Q_t-Q_0)/(Q_e-Q_0)]$ versus square root of time produced a straight line in a short time period. The slope of the kinetic adsorption curve can be used to calculate the diffusion time constant (D/r_2), which was based on Fick's law (see Supporting Information) and summarized in Table S4. It was found that the diffusion time constants (D/r_2) for all investigated samples were well within the scale

of 10^{-3} s^{-1}, indicating that the diffusion process in these as-synthesized MEL zeolites was dominated by a combination of both intracrystalline and inter-crystal diffusion.[39,40]

Schematic illustrations for these two distinct diffusion pathways (i.e., path 1: intra-crystal diffusion; path 2: inter-crystal diffusion) over either conventional or hierarchical MEL zeolites were shown in Fig. 6c and Fig. 6d, respectively. In general, the inter-crystal diffusion is much faster than the intra-crystal diffusion that is performed through the complicated porous network due to the limited mass transport. For P-MEL@Fe with solely micropores (Fig. 6c), molecular diffusion across the inter-crystal surface of MEL zeolites (path 2) dominated, together with a larger D/r_2 value, as shown in Table S4. For hierarchical H-MEL-31 and H-MEL@Fe-20 zeolites with highly interconnected and open mesopores (Fig. 6d), the intra-crystal molecular diffusion (path 1) was largely promoted along with a reduced D/r_2 value (Table S4). Interestingly, such a marked difference in molecular diffusion between conventional and hierarchical MEL zeolites over nonpolar benzene was found to be totally absent for experiments carried out over polar toluene, where enhanced inter-crystal diffusion and a larger D/r_2 value was observed. This indicated that the chemical environment of the internal pore walls of hierarchical MEL zeolites favored the interaction with nonpolar adsorbates and associated intra-crystal molecular diffusion.

Catalytic activity

To evaluate the catalytic performance of resultant MEL zeolites, the alkylation of mesitylene with benzyl alcohol was carried out, which was an important reaction for

the production of fine chemicals and pharmaceutical intermediates.[1] According to previous reports,[41,42] the kinetic diameter of mesitylene (0.87 nm) was obviously larger than the micropore size in MEL zeolite. For the liquid benzylation of mesitylene,[5] it was well known that both the alkylation of mesitylene and self-etherification of benzyl alcohol can be catalyzed by either Lewis or Brønsted acid sites on the internal/external surfaces of (hierarchical) MEL zeolite. Thus, the alkylation reaction between mesitylene with benzyl alcohol taked place exclusively on the external surface of conventional microporous MEL zeolite particles, while self-etherification occurred on both the external surface and the much more abundant internal surface of pore walls simultaneously. In contrast, the hierarchical single-crystalline MEL zeolite adopted highly open and interconnected mesopores, which allowed for intra-crystal diffusion of the bulky mesitylene molecules. As shown in Fig. 7a, for the P-MEL zeolite, no conversion of benzyl alcohol was observed after 30 h, indicating that P-MEL did not have any activity in the alkylation reaction owing to the absence of acidity. While H-MEL-31 showed an increasing conversion of benzyl alcohol with reaction time, suggesting that the acid sites were active species. Interesting, the integration of both solid acid and Fe-oxy redox sites in such a hierarchical MEL zeolite can further enhance the activity against benzyl alcohol, due to the involvement of Fe^{3+}/Fe^{2+} redox pairs in the well-accepted redox mechanism for benzylation of mesitylene (Scheme S1).[20]

From the perspective of product selectivity, the target product 2-benzyl-1,3,5-trimethylbenzene (BTMB) from the alkylation of mesitylene was

greatly favored over the hierarchical H-MEL-31 zeolite together with an inhibited self-etherification side reaction that produced dibenzyl ether (Fig. 7b). The explanation for this was straightforward and two-fold: i) the highly open and interconnected mesopores with large surface areas accommodated the bulky mesitylene and BTMB molecules to promote the target alkylation reaction; ii) the remarkably decreased affinity of pore walls to polar adsorbates further reduced the concentration of benzyl alcohol in the porous network and inhibited the self-etherification side reaction. Notably, based on the reaction cycles[20] (Fig. 7c) and the much faster self-etherification side reaction, a short "induction period" with a low BTMB selectivity was observed before the quasi-equilibrium steady state was reached, when dibenzyl ether also worked as an alkylating agent[3] towards a high and stable BTMB selectivity (Fig. S12). Interestingly, we observed a decrease in BTMB selectivity for the acid-redox co-functionalized MEL zeolite despite the significantly increased conversion of benzyl alcohol (Fig. 7b, Fig. S13 and Fig. S14). As we all know, Fe-containing solid catalysts possessed redox properties ($Fe^{3+} + e^- \Leftrightarrow Fe^{2+}$), which dominated the benzylation reaction regardless of catalysts acidity.[19] In other words, the incorporation of Fe^{3+} species in the zeolite framework greatly enhanced the activity of benzyl alcohol, resulting in the formation of benzyl carbocation, which was quickly transformed into dibenzyl ether. However, the dibenzyl ether must be hydrolyzed to form benzyl alcohol, and then it can participate in the alkylation with mesitylene to produce BTMB. However, the hydrolysis rate for dibenzyl ether was considered to be slower than the generation of dibenzyl ether,[43] leading to the

accumulation of dibenzyl ether, which reduced the selectivity of BTMB for Fe-containing MEL zeolites. The whole transformation process for benzyl carbocation was depicted in Fig. 7d, which clearly illustrated the transition pathway for benzyl carbocation arising from the activation of benzyl alcohol over combined solid acid and redox sites.[44] In addition, a leaching test for a typical catalyst corroborated the hypothesis that the acid-redox co-functionalized MEL zeolites exhibited excellent stability against metal leaching (Fig. S15).

Coke analysis

A part of the spent catalysts was taken for thermogravimetric analysis (TGA) to investigate the coke formed in MEL zeolites. Figure S16 showed the weight loss curves for spent H-MEL-31, P-MEL@Fe and H-MEL@Fe-20 samples, which exhibited three distinct regions of weight loss for all samples in the temperature ranges of 25–150 °C, 150–350 °C and 350–700 °C, respectively. Generally, the weight loss below 150 °C was attributed to the moisture and adsorbed water in zeolite cavities and channels.[45] The mass loss observed in the temperature range of 150–350 °C was assigned to soft coke that occurred at a moderate temperature and can be extracted by organic solvent,[46] and the weight loss for H-MEL-31, P-MEL@Fe and H-MEL@Fe-20 in the temperature range of 350–700 °C can be classified as hard coke or insoluble coke. It was worth noting that the proportion of hard coke in the total coke for H-MEL-31, P-MEL@Fe and H-MEL@Fe-20 was approximately 35 %, 27 % and 48 %, respectively. Therefore, we deduced that the coke formed during the alkylation of mesitylene with benzyl alcohol over the investigated MEL zeolite

catalysts was mainly composed of soft coke.[47]

To further investigate the composition of the soluble coke on the used catalyst, the soft coke in H-MEL-31, P-MEL@Fe and H-MEL@Fe-20 was extracted by 1,3,5-trimethylcyclohexane and subsequently analyzed by GC-MS,[47,48] as shown in Fig. S17. It was observed that these soft cokes were mainly composed of raw materials, solvents, products and internal standard substances (dodecane); the polyaromatics and multimethybenzenes were not detected, which was in agreement with TGA analysis that showed that the main coke was soluble coke.

Conclusions

In summary, we propose here a simple and general strategy to fabricate acid-redox co-functionalized hierarchical single crystal MEL zeolites with well-evaluated mesoporosity in terms of surface openness, pore interconnectivity and adsorbate-specific pore adaptability. This strategy works well for a hierarchical MEL zeolite system that simultaneously integrates solid acid and Fe-oxy redox sites, which exhibits greatly enhanced catalytic activity and stability towards benzylation of mesitylene. Mechanistic insights are provided showing that the superior catalytic performance originates from enhanced intra-crystal molecular diffusion, mitigated metal leaching and optimized adsorbate-pore wall interactions.

Associated content

Supporting Information

Experimental content for characterization of MEL zeolites; study of catalytic and diffusion performance of synthesized MEL zeolites; additional SEM, XPS, UV-vis, EPR, ^{27}Al MAS NMR,

FTIR, TEM, N_2 isotherm data, TGA and GC-MS analysis.

Acknowledgments

This work was supported by the Natural Science Foundation of China (No. 21978055 and 21808040), the Science and Technology Program of Guangzhou, China (201804010172) and "High-level Talents Program" of Pearl River (2017GC010080). Y. Zhu acknowledges the financial support from the National Natural Science Foundation of China (Grant No. 21771161) and Thousand Talents Program for Distinguished Young Scholars.

References

1. Li B, Leng K, Zhang Y, et al. Metal–Organic Framework Based upon the Synergy of a Brønsted Acid Framework and Lewis Acid Centers as a Highly Efficient Heterogeneous Catalyst for Fixed-Bed Reactions. *J. Am. Chem. Soc.* 2015;137(12):4243-4248.
2. Huang J, Liu B, Liao Z, Chen H, Yan K. Fabrication of Cu-Encapsulated Hierarchical MEL Zeolites for Alkylation of Mesitylene with Benzyl Alcohol. *Ind. Eng. Chem. Res.* 2019;58(36):16636-16644.
3. Jin H, Ansari MB, Jeong E-Y, Park S-E. Effect of mesoporosity on selective benzylation of aromatics with benzyl alcohol over mesoporous ZSM-5. *J. Catal.* 2012;291:55-62.
4. Hwang YK, Chang J-S, Park S-E, et al. Microwave Fabrication of MFI Zeolite Crystals with a Fibrous Morphology and Their Applications. *Angew. Chem.Int. Ed.* 2005;44(4):556-560.
5. Yuan B, Li Y, Wang Z, Yu F, Xie C, Yu S. A Novel Brønsted-Lewis acidic catalyst based on heteropoly phosphotungstates: Synthesis and catalysis in benzylation of p-xylene with benzyl alcohol. *Mol. Catal.* 2017;443:110-116.
6. Pérez-Ramírez J, Christensen CH, Egeblad K, Christensen CH, Groen JC. Hierarchical zeolites: enhanced utilisation of microporous crystals in catalysis by advances in materials design. *Chem. Soc. Rev.* 2008;37(11):2530-2542.
7. Hartmann M, Machoke AG, Schwieger W. Catalytic test reactions for the evaluation of hierarchical zeolites. *Chem. Soc. Rev.* 2016;45(12):3313-3330.
8. Wei Y, Parmentier TE, de Jong KP, Zecevic J. Tailoring and visualizing the pore architecture of hierarchical zeolites. *Chem. Soc. Rev.* Oct 21 2015;44(20):7234-7261.
9. Liu B, Ren Y, Duan Q, Chen F, Xi H, Qian Y. Facile synthesis of mesoporous aluminosilicates constructed with crystalline microporous frameworks. *Appl. Surf. Sci.* 2013;279:55-61.
10. Dai C, Zhang A, Liu M, Gu L, Guo X, Song C. Hollow Alveolus-Like Nanovesicle Assembly with Metal-Encapsulated Hollow Zeolite Nanocrystals. *ACS nano.* 2016;10(8):7401-7408.
11. Pagis C, Morgado Prates AR, Farrusseng D, Bats N, Tuel A. Hollow Zeolite Structures: An Overview of Synthesis Methods. *Chem. Mater.* 2016;28(15):5205-5223.

12. Zhang F, Yan Y, Yang H, et al. Understanding Effect of Wall Structure on the Hydrothermal Stability of Mesostructured Silica SBA-15. *J. Phys. Chem. B.* 2005;109(18):8723-8732.
13. Zhu J, Zhu Y, Zhu L, et al. Highly Mesoporous Single-Crystalline Zeolite Beta Synthesized Using a Nonsurfactant Cationic Polymer as a Dual-Function Template. *J. Am. Chem. Soc.* 2014;136(6):2503-2510.
14. Zhang Q, Mayoral A, Terasaki O, et al. Amino Acid-Assisted Construction of Single-Crystalline Hierarchical Nanozeolites via Oriented-Aggregation and Intraparticle Ripening. *J. Am. Chem. Soc.* 2019;141(9):3772-3776.
15. Tao S, Li X, Wang X, et al. Facile Synthesis of Hierarchical Nanosized Single-Crystal Aluminophosphate Molecular Sieves from Highly Homogeneous and Concentrated Precursors. *Angew. Chem. Int. Ed.* 2020;59(9):3455-3459.
16. Milina M, Mitchell S, Crivelli P, Cooke D, Pérez-Ramírez J. Mesopore quality determines the lifetime of hierarchically structured zeolite catalysts. *Nat. Commun.* 2014;5(1):3922.
17. Zubiaga A, Warringham R, Boltz M, et al. The assessment of pore connectivity in hierarchical zeolites using positron annihilation lifetime spectroscopy: instrumental and morphological aspects. *Phys. Chem. Chem. Phys.* 2016;18(13):9211-9219.
18. Coq B, Gourves V, Figuéras F. Benzylation of toluene by benzyl chloride over protonic zeolites. *Appl. Catal., A.* 1993;100(1):69-75.
19. Choudhary VR, Jana SK, Mamman AS. Benzylation of benzene by benzyl chloride over Fe-modified ZSM-5 and H-β zeolites and Fe2O3 or FeCl3 deposited on micro-, meso- and macro-porous supports. *Microporous Mesoporous Mater.* 2002;56(1):65-71.
20. Salavati-Niasari M, Hasanalian J, Najafian H. Alumina-supported FeCl3, MnCl2, CoCl2, NiCl2, CuCl2, and ZnCl2 as catalysts for the benzylation of benzene by benzyl chloride. *J. Mol. Catal. A: Chem.* 2004;209(1):209-214.
21. Knapp C, Obuchi A, Uchisawa JO, Kushiyama S, Avila P. Method for selective removal of supported platinum particles from external zeolite surfaces: characterisation of and application to a catalyst for the selective reduction of nitrogen oxide by hydrocarbons. *Microporous Mesoporous Mater.* 1999;31(1):23-31.
22. Wu Z, Goel S, Choi M, Iglesia E. Hydrothermal synthesis of LTA-encapsulated metal clusters and consequences for catalyst stability, reactivity, and selectivity. *J. Catal.* 2014;311:458-468.
23. Zhao X, Wang X. Characterizations and Catalytic Properties of Chromium Silicalite-2 Prepared by Direct Hydrothermal Synthesis and Impregnation. *Catal. Lett.* 2010;135(3-4):233-240.
24. Gomez S, Lerici L, Saux C, et al. Fe/ZSM-11 as a novel and efficient photocatalyst to degrade Dichlorvos on water solutions. *Appl. Catal., B.* 2017;202:580-586.
25. Tan P. Active phase, catalytic activity, and induction period of Fe/zeolite material in nonoxidative aromatization of methane. *J. Catal.* 2016;338:21-29.
26. Zhang D, Yang RT. N2O Formation Pathways over Zeolite-Supported Cu and Fe Catalysts in NH3-SCR. *Energy Fuels.* 2018;32(2):2170-2182.
27. Yang Y, Zhang H, Yan Y. The preparation of Fe2O3-ZSM-5 catalysts by metal-organic chemical vapour deposition method for catalytic wet peroxide oxidation of m-cresol. *Roy. Soc. Open. Sci.* 2018;5(3):171731.
28. Chen Y, Li C, Chen X, Liu Y, Tsang C-W, Liang C. Synthesis and Characterization of Iron-Substituted ZSM-23 Zeolite Catalysts with Highly Selective Hydroisomerization of n-Hexadecane. *Ind. Eng. Chem. Res.* 2018;57(41):13721-13730.

29. Pérez Vélez R, Ellmers I, Huang H, et al. Identifying active sites for fast NH3-SCR of NO/NO2 mixtures over Fe-ZSM-5 by operando EPR and UV–vis spectroscopy. *J. Catal.* 2014;316:103-111.
30. Alzeer MIM, MacKenzie KJD, Keyzers RA. Facile synthesis of new hierarchical aluminosilicate inorganic polymer solid acids and their catalytic performance in alkylation reactions. *Microporous Mesoporous Mater.* 2017;241:316-325.
31. Yutthalekha T, Wattanakit C, Warakulwit C, et al. Hierarchical FAU-type zeolite nanosheets as green and sustainable catalysts for benzylation of toluene. *J. Clean. Prod.* 2017;142:1244-1251.
32. Abelló S, Bonilla A, Pérez-Ramírez J. Mesoporous ZSM-5 zeolite catalysts prepared by desilication with organic hydroxides and comparison with NaOH leaching. *Appl. Catal., A.* 2009;364(1):191-198.
33. Wang S, Wang P, Qin Z, et al. Relation of Catalytic Performance to the Aluminum Siting of Acidic Zeolites in the Conversion of Methanol to Olefins, Viewed via a Comparison between ZSM-5 and ZSM-11. *ACS Catal.* 2018;8(6):5485-5505.
34. Bleken F, Skistad W, Barbera K, et al. Conversion of methanol over 10-ring zeolites with differing volumes at channel intersections: comparison of TNU-9, IM-5, ZSM-11 and ZSM-5. *Phys. Chem. Chem. Phys.* 2011;13(7):2539-2549.
35. Lyu J-H, Hu H-L, Rui J-Y, et al. Nitridation: A simple way to improve the catalytic performance of hierarchical porous ZSM-5 in benzene alkylation with methanol. *Chin. Chem. Lett.* 2017;28(2):482-486.
36. Candu N, Florea M, Coman SM, Parvulescu VI. Benzylation of benzene with benzyl alcohol on zeolite catalysts. *Appl. Catal., A.* 2011;393(1-2):206-214.
37. Seo Y, Cho K, Jung Y, Ryoo R. Characterization of the Surface Acidity of MFI Zeolite Nanosheets by 31P NMR of Adsorbed Phosphine Oxides and Catalytic Cracking of Decalin. *ACS Catal.* 2013;3(4):713-720.
38. Zhao Z, Li Z, Lin YS. Adsorption and Diffusion of Carbon Dioxide on Metal−Organic Framework (MOF-5). *Ind. Eng. Chem. Res.* 2009;48(22):10015-10020.
39. Li C, Ren YQ, Gou JS, Liu BY, Xi HX. Facile synthesis of mesostructured ZSM-5 zeolite with enhanced mass transport and catalytic performances. *Appl. Surf. Sci.* 2017;392:785-794.
40. Qi X, Vattipalli V, Dauenhauer PJ, Fan W. Silica Nanoparticle Mass Transfer Fins for MFI Composite Materials. *Chem. Mater.* 2018;30(7):2353-2361.
41. Emdadi L, Wu Y, Zhu G, et al. Dual Template Synthesis of Meso- and Microporous MFI Zeolite Nanosheet Assemblies with Tailored Activity in Catalytic Reactions. *Chem. Mater.* 2014;26(3):1345-1355.
42. Emdadi L, Oh SC, Wu Y, et al. The role of external acidity of meso-/microporous zeolites in determining selectivity for acid-catalyzed reactions of benzyl alcohol. *J. Catal.* 2016;335:165-174.
43. Mantri K, Komura K, Kubota Y, Sugi Y. Friedel–Crafts alkylation of aromatics with benzyl alcohols catalyzed by rare earth metal triflates supported on MCM-41 mesoporous silica. *J. Mol. Catal. A: Chem.* 2005;236(1):168-175.
44. Choudhary V, Jana S, Mamman A. Benzylation of benzene by benzyl chloride over Fe-modified ZSM-5 and H-β zeolites and Fe2O3 or FeC13 deposited on micro-, meso- and macro-porous supports. *Microporous Mesoporous Mater.* 2002;56:65–71.

45. Trnik A, Scheinherrova L, Medved I, Cerny R. Simultaneous DSC and TG analysis of high-performance concrete containing natural zeolite as a supplementary cementitious material. *J Therm Anal Calorim.* 2015;121(1):67-73.
46. Gou J, Wang Z, Li C, et al. The effects of ZSM-5 mesoporosity and morphology on the catalytic fast pyrolysis of furan. *Green Chem.* 2017;19(15):3549-3557.
47. Li J, Xiang H, Liu M, Wang Q, Zhu Z, Hu Z. The deactivation mechanism of two typical shape-selective HZSM-5 catalysts for alkylation of toluene with methanol. *Catal. Sci. Technol.* 2014;4(8):2639-2649.
48. Liu Y, Zou Y, Jiang H, Gao H, Chen R. Deactivation mechanism of beta-zeolite catalyst for synthesis of cumene by benzene alkylation with isopropanol. *Chin. J. Chem. Eng.* 2017;25(9):1195-1201.

Figure Captions

Figure.1 XRD patterns of different MEL zeolite samples.

Figure.2 (a) HAADF-STEM image and elemental distributions of H-MEL@Fe-20 by EDS mapping. HRTEM image of the single-crystalline hierarchical H-MEL@Fe-20 zeolite (b) containing faceted intracrystalline mesopores, and (c) containing pore walls along [100] direction. FFT pattern is embedded. (d) Contrast-transfer-function (CTF) corrected image (at a defocus of -230 nm) with overlaid simulated projected potential map (with a point-spread-function width of 1.8 Å) and structural projections of H-MEL-31 zeolite along [100] direction.

Figure.3 (a) Reconstructed volume by electron tomography, (b) Volume with labelled mesopores embedded and rendered in diverse colors, (c-f) Labelled mesopores classified by different mesopore volume (from left to right: $> 3 \times 10^4$ nm^3, $1 \sim 3 \times 10^4$ nm^3, $1 \sim 10 \times 10^3$ nm^3 and $1 \sim 10 \times 10^3$ nm^3), (g) mesopores open to the surface and (h) sequential slices of the reconstructed volume with an interval of 10 nm for H-MEL-31; the red arrow shows the mesopore interconnectivity among slices (i) A statistical analysis of mesopore volume distribution over different equivalent spherical pore size. Red and blue bars refer to constricted/closed and open mesopores respectively.

Figure.4 (a) Positron annihilation lifetime spectroscopy lifetime spectra and (b) corresponding lifetime components and relative fractions for P-MEL and H-MEL-31 zeolites.

Figure.5 The crystal structure model of various T-sites in MEL lattice.

Figure.6 Plots of the fractional adsorption uptakes $[(Q_t-Q_0)/(Q_e-Q_0)]$ of benzene (a),toluene (b) against the square root of adsorption time, and proposed diffusion path of benzene/toluene molecules during adsorption over (c) P-MEL@Fe and (d) H-MEL-31/H-MEL@Fe-20 samples.

Figure.7 (a) Conversion of benzyl alcohol and (b) selectivity of BTMB with time-on-stream on synthesized zeolites; (c) the proposed reaction networks and (d) scheme showing the transformation of benzyl carbocation.

Scheme 1 Synthetic Strategy for Fe immobilized hierarchical single-crystalline MEL zeolites.

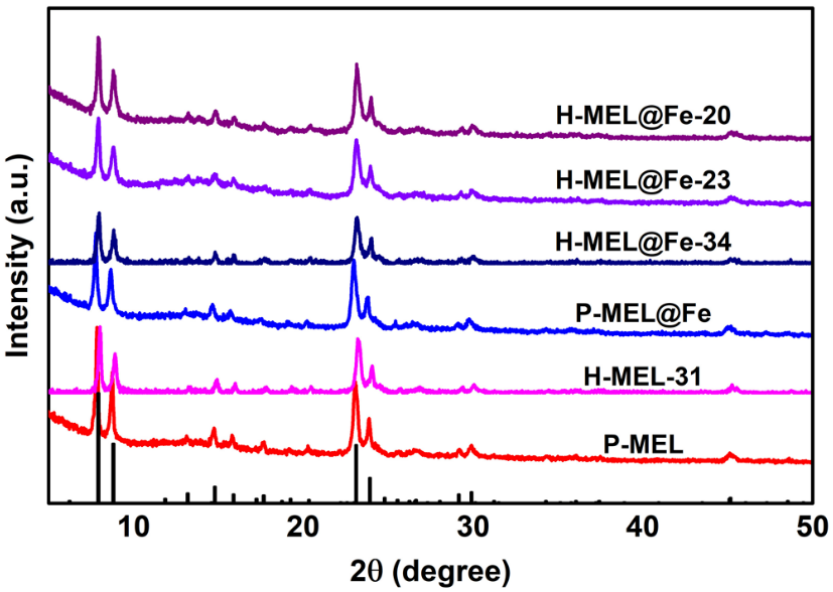

Figure 1. XRD patterns of different MEL zeolite samples.

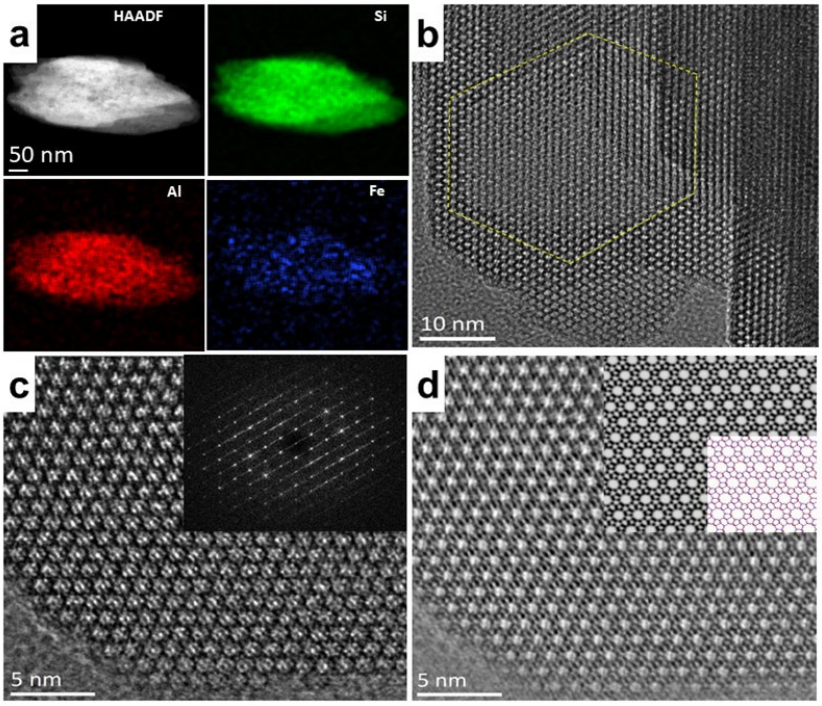

Figure 2. (a) HAADF-STEM image and elemental distributions of H-MEL@Fe-20 by EDS mapping. HRTEM image of the single-crystalline hierarchical H-MEL@Fe-20 zeolite (b) containing faceted intracrystalline mesopores, and (c) containing pore walls along [100] direction. FFT pattern is embedded. (d) Contrast-transfer-function (CTF) corrected image (at a defocus of -230 nm) with overlaid simulated projected potential map (with a point-spread-function width of 1.8 Å) and structural projections of H-MEL-31 zeolite along [100] direction.

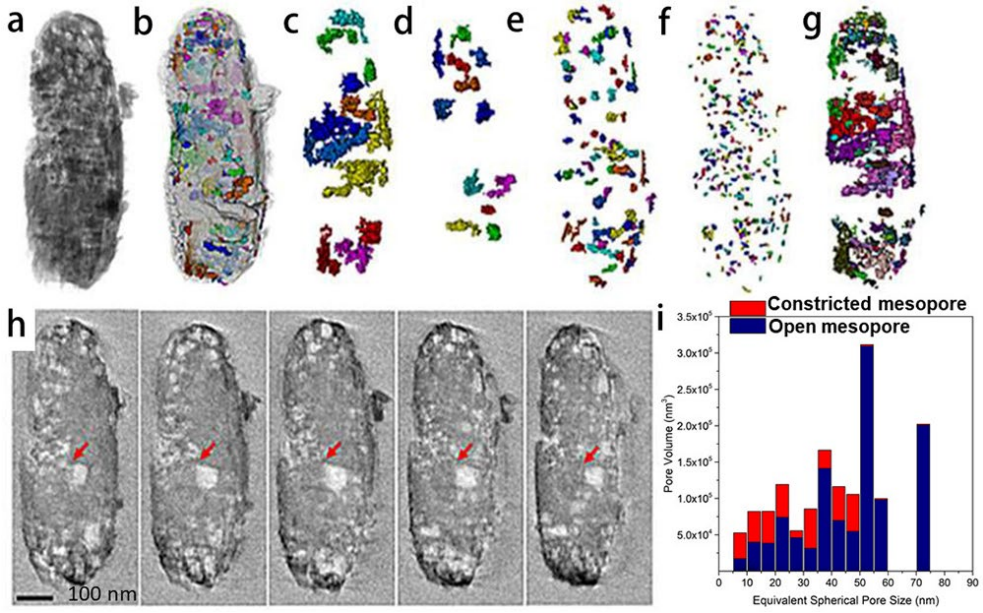

Figure 3. (a) Reconstructed volume by electron tomography, (b) Volume with labelled mesopores embedded and rendered in diverse colors, (c-f) Labelled mesopores classified by different mesopore volume (from left to right: $> 3 \times 10^4$ nm^3, $1 \sim 3 \times 10^4$ nm^3, $1 \sim 10 \times 10^3$ nm^3 and $1 \sim 10 \times 10^3$ nm^3), (g) mesopores open to the surface and (h) sequential slices of the reconstructed volume with an interval of 10 nm for H-MEL-31; the red arrow shows the mesopore interconnectivity among slices (i) A statistical analysis of mesopore volume distribution over different equivalent spherical pore size. Red and blue bars refer to constricted/closed and open mesopores respectively.

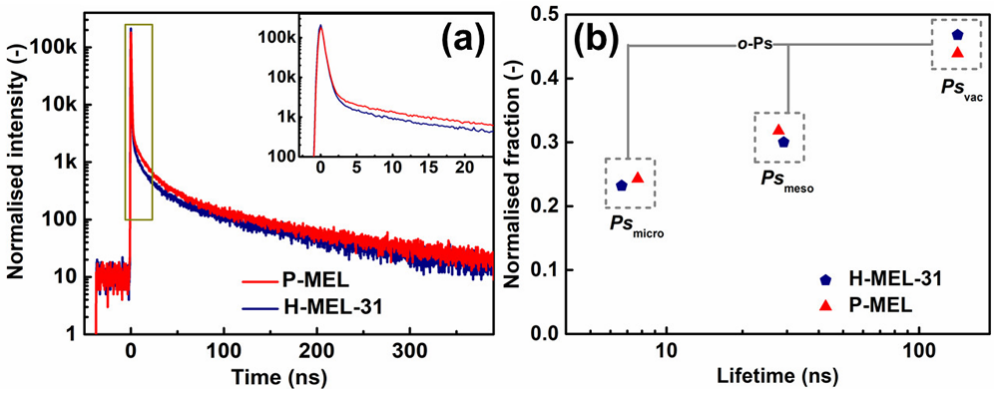

Figure 4. (a) Positron annihilation lifetime spectroscopy lifetime spectra and (b) corresponding lifetime components and relative fractions for P-MEL and H-MEL-31 zeolites.

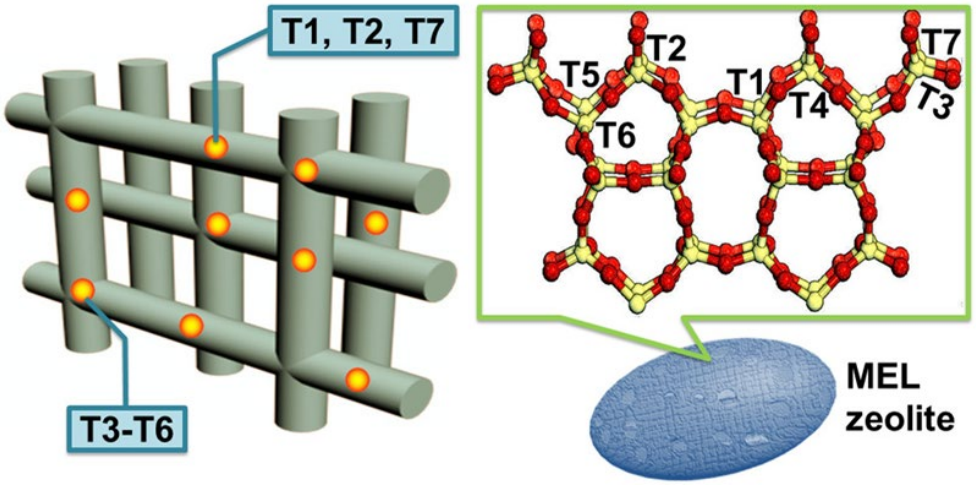

Figure 5. The crystal structure model of various T-sites in MEL lattice.

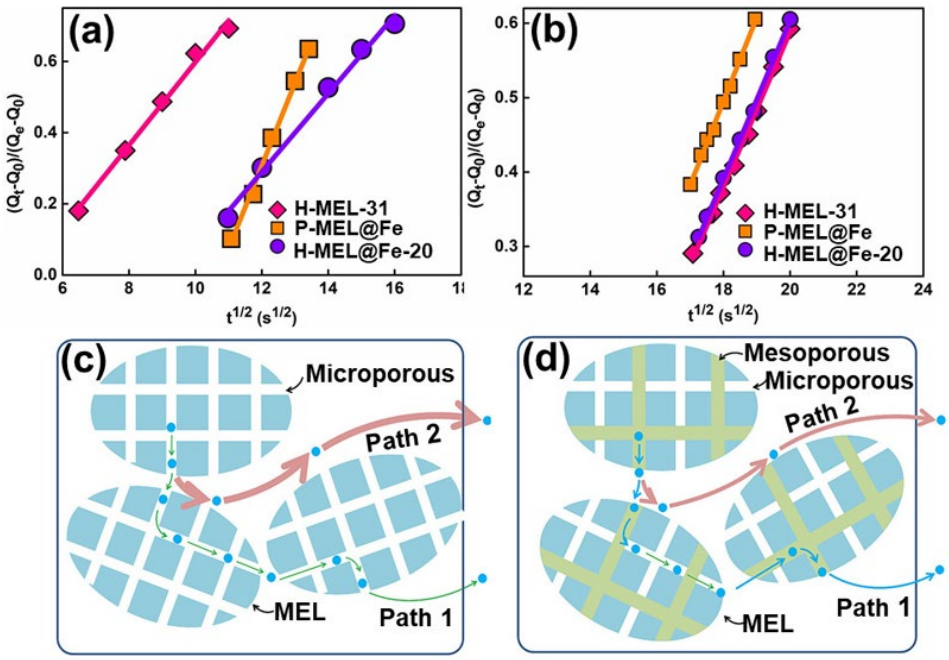

Figure 6. Plots of the fractional adsorption uptakes [$(Q_t-Q_0)/(Q_e-Q_0)$] of benzene (a),toluene (b) against the square root of adsorption time, and proposed diffusion path of benzene/toluene molecules during adsorption over (c) P-MEL@Fe and (d) H-MEL-31/H-MEL@Fe-20 samples.

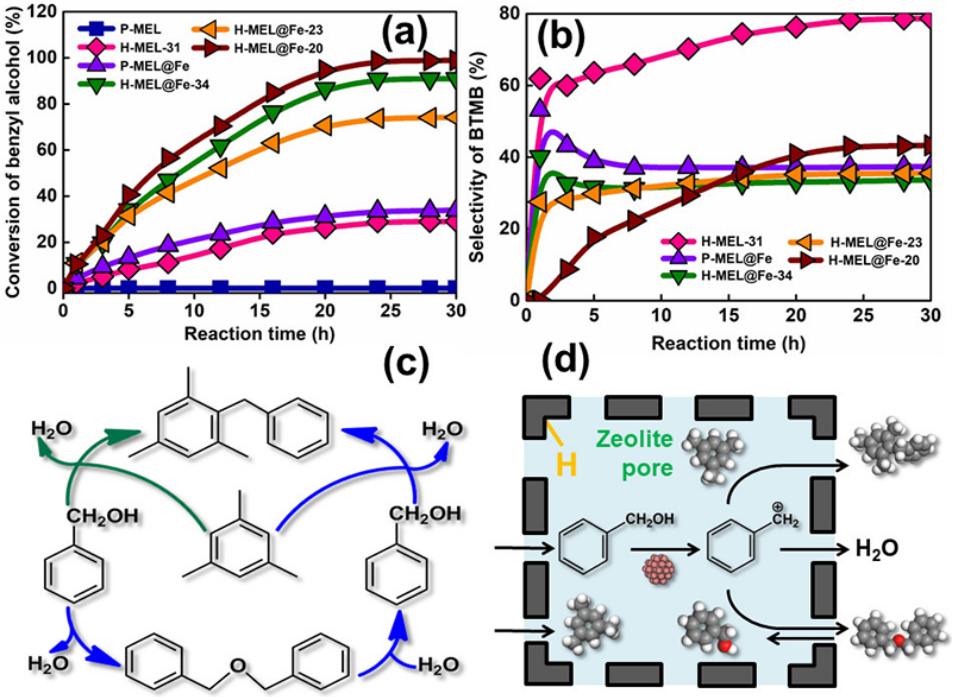

Figure 7. (a) Conversion of benzyl alcohol and (b) selectivity of BTMB with time-on-stream on synthesized zeolites; (c) the proposed reaction networks and (d) scheme showing the transformation of benzyl carbocation.

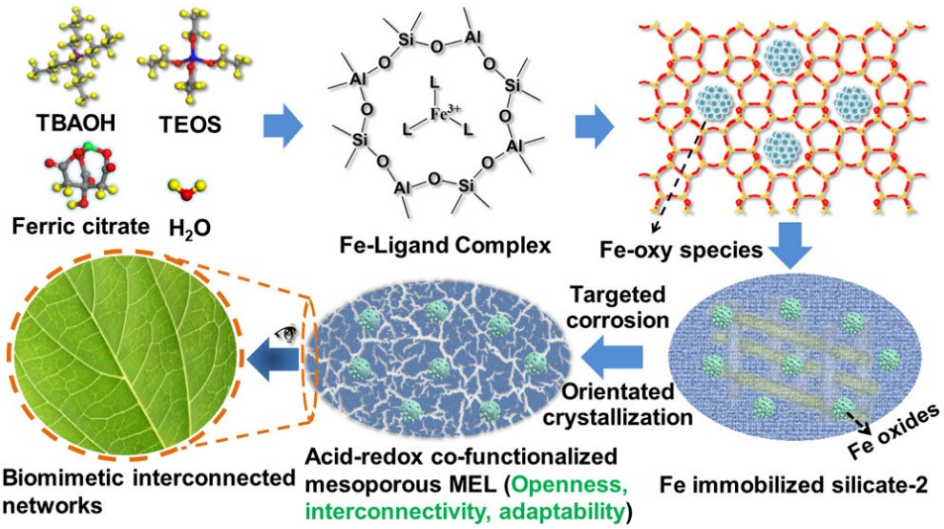

Scheme 1. Synthetic Strategy for Fe immobilized hierarchical single-crystalline MEL zeolites.